FULL RESEARCH ARTICLE

Towards an understanding of the functional properties of NiTi produced by powder bed fusion

Adelaide Nespoli[1] · Antonio Mattia Grande[2] · Nicola Bennato[1] · Daniela Rigamonti[2] · Paolo Bettini[2] · Elena Villa[1] · Giuseppe Sala[2] · Francesca Passaretti[1]

Abstract

In this work, near fully dense NiTi components have been fabricated using a 55.2Ni-Ti (wt.%) powder through selective laser beam melting. The effect of the manufacturing process on mechanical and functional properties of the selected NiTi alloy has been systematically investigated by tuning the hatching distance, h, and the scanning speed, v, in order to define a set of 12 NiTi families. The as-built NiTi parts present phase transformation temperatures higher than those of the feedstock, ascribed to the depletion of Ni during the process. Pseudoelasticity and shape memory responses have been evaluated through uniaxial compression and bending measurements, respectively. Both quasi-static and dynamic analyses have been considered. It is shown that the resulting material may exhibit distinct damping and strain recovery responses depending on the used process parameters.

Keywords Additive manufacturing · powder bed fusion · NiTi · Pseudoelasticity · Shape memory alloys · Damping

1 Introduction

Nickel-Titanium (NiTi) alloys are known for their pseudoelastic and shape memory mechanical behaviors, which occur following a first-order and reversible thermo-elastic transformationbetween two solid phases, austenite and martensite stable at high and low temperatures, respectively. These two mechanical responses are mainly attributed to the Ni–Ti ratio and secondly to the thermo-mechanical history of the material; both aspects influence the phase transformation temperatures of the alloy and consequently determining the functional properties of the material [1]. The main characteristic of NiTi is the ability to reach and recover high deformations when subject to a thermal cycle under load (shape memory effect) or during a loading/unloading cycle at constant temperature (pseudoelasticity). In both cases, the resulting mechanical work has been exploited in practical applications as actuators and sensors [2, 3], spanning from aerospace to biomedical industries [4, 5]. Lightness, compactness, noiseless and thermo-mechanical cyclic stability are the leading characteristics of NiTi-based devices [6]. However, the poor workability by means of conventional processing techniques limits the use of NiTi; a poor workpiece quality and a rather simple final geometry that often is in the form of wires, springs or tapes [7, 13], are the two main concerns deriving from the difficult processing.

In recent years, additive manufacturing has proven to be an alternative production process of many metal alloys [14]. As opposed to subtractive technologies, it uses material only where it is needed and allows extending the freedom of design and manufacturing of complex structures in a single fabrication step. In particular, according to ISO/ASTM 52,900, Laser Beam Melting (LBM), also known with the name of Selective Laser Melting (SLM), is a powder bed fusion process that uses a laser beam source to selectively melt metal micrometric powder, layer by layer following a 3D CAD model. It allows producing three-dimensional objects limiting the use of tools and overcoming the problems related to traditional technologies [15].

One of the main advantages is the possibility to produce net-shape or near-net-shape components that can potentially expand the field of applications of NiTi [16, 20]. At present,

✉ Adelaide Nespoli
    adelaide.nespoli@cnr.it

1   Consiglio Nazionale Delle Ricerche, Istituto Di Chimica Della Materia Condensata E Di Tecnologie Per L'Energia (CNR-ICMATE), via G. Previati 1/e, 23900 Lecco, Italy

2   Dipartimento Di Scienze E Tecnologie Aerospaziali, Politecnico Di Milano, via La Masa 34, 20156 Milano, Italy

the great part of the works concerning the production of NiTi parts by LBM, deals with the study of the effects of the process parameters on the microstructure and the thermo-mechanical response [21, 25]. With this regard, the laser energy input is one of the main criteria as it counts for the main process parameters. The laser energy density E of a continuous wave emission laser is often evaluated according to the following simplified relationship [26]:

$$E = \frac{P}{h \cdot v \cdot l} \tag{1}$$

where P is the laser power, v is the scanning speed, l is the layer thickness, h is the hatching distance. For NiTi alloys, values of E in the range of 55–222 J/mm^3 provide high density and low porosity level within the produced samples [22, 25, 27, 29, 31]. Some selective laser melting machines use pulse wave emission laser, which present unique process parameters due to the laser pulse mechanism [32–34]. For these devices, the laser energy density can be approximated to [35]:

$$E = \frac{P \cdot t}{h \cdot d \cdot l} \tag{2}$$

where t is the exposure time and d is the point distance.

Among the main works on this topic, Haberland et al. [22], Saedi et al. [28] and Walker et al. [21] studied different compositions of NiTi. Haberland [22] investigated NiTi alloys, from shape memory to pseudoelastic, and found that the phase transformation temperatures increase with the increasing of E. It was established that a minimum E of about 200 J/mm^3 is required to fully consolidate the material and that the process parameters need to be adjusted to have E as low as possible. So, a set of optimized process parameters was defined: 77 W (P), 200 mm/s (v), 120 μm (h), 50 μm (l), which gave a laser energy density of 234 J/mm^3. The effects of post-processing, such as solubilization and aging were also reported. Saedi [28] focused on NiTi with 50.8 at% of Ni and on one set of process parameters: 250 W (P), 1250 mm/s (v), 120 μm (h), 30 μm (l), which result in a laser energy density of 55.5 J/mm^3. They solubilized samples and tested two aging temperatures through micro-hardness, compression and strain recovery measurements. Walker et al. [21] studied a NiTi alloy with 50.09 at% of Ni. It was evaluated the effect of both a high and a low energy input by varying the laser power P between 45 and 300 W and the scanning speed v between 100 and 3000 mm/s. It was found that when P is held constant, the relative density of the printed parts decreases with the increasing of v. Based on their results, they defined an optimum set of process parameters (same as the ones presented in [28]): 250 W (P), 1250 mm/s (v), 120 μm (h), 30 μm (l), which gave a laser energy density of 55.5 J/mm^3. They found an

increase of the phase transformation temperatures after the laser beam melting process ascribed to Ni evaporation and established that the shift of the temperatures increases with the increasing of E.

Furthermore, changes of the phase transformation temperatures and consequently of the final functional performances of the printed part were observed in [23]; these changes were attributed to a change of the microstructure of the final part with respect to the NiTi powder.

During laser beam melting process, the metal undergoes to extremely rapid super-heating and under-cooling, generating ultrafine microstructure and high residual stresses inside the as-built material. As recently reported [26], the change of microstructure of NiTi produced through selective laser beam melting process is related to one or more the following causes: Ni loss by evaporation, oxygen pickup, precipitation, strong texture, high density of dislocations, residual stresses, inhomogeneous grain size distribution and microstructural heterogeneity. Therefore, a deep understating of the link between the process and both thermal and functional properties is fundamental to produce reliable components with the desired properties.

In this view, this research systematically studies functional and thermo-mechanical properties of different NiTi specimens fabricated by selective laser beam melting. At first, a large set of process parameters was selected to produce near fully dense parts and avoid discontinuous structures and irregular track morphology. To this end, families with identical laser power, P, and layer thickness, l, but different h and scanning speed v parameters have been considered. Therefore, a matrix of (h, v) values was defined and used to understand and to deepen the variation of the microstructure, the phase transformation temperatures and the mechanical response of NiTi parts. A thermal-treatment based on solubilization at high temperature was also adopted to tune and homogenize the microstructure of the processed material. Dynamic study and damping response were investigated to explore the link between processing, post-processing and functional properties of the selected NiTi alloy.

2 Material and methods

Gas atomized NiTi powder was manufactured and supplied by TLS Technik GmbH & Co. Spezialpulver KG (Bitterfeld, Germany). Particles have spherical shape (provided diameter < 45 μm) and chemical composition as reported in Table 1. SEM images of the received powder are reported in Appendix A.

NiTi parts were produced by a Renishaw AM400 machine operating with a 400 W fiber laser in pulsed wave emission and producing a spot diameter of approximately 70 μm at the focal point. Prior to processing, vacuum was applied (oxygen

Table 1 Elemental composition of NiTi powder (wt.%)

Ti	Ni	C	O	N	H
bal	55.2	0.005	0.069	0.0025	<0.001

level lower than 500 ppm), and the build chamber was filled with Argon. No preheating was applied to the build platform.

Rectangular bars, $3 \times 3 \times 15$ mm^3, were produced with a meander strategy in a reduced build volume (RBV, $78 \times 78 \times 55$ mm^3). The parts were produced directly on a Ti-based platform with the main axis parallel to the z axis of the machine; in place of the supports, each specimen was designed with a 1×1 mm^2 tip end. A CAD model and a sketch of the NiTi bars and of the production run are reported in Fig. 1.

During the manufacturing process, the laser power P, the laser point distance d and the layer thickness l were kept constant at 250 W, 60 µm and 30 µm, respectively. Besides, three laser exposure times were considered: 60, 48 and 40 µs. Therefore, the laser speed, calculated as the ratio between the laser exposure distance d and the laser exposure time t, were 1000, 1250, 1500 mm/s, respectively. Moreover, four hatching distance values were selected: 50, 75, 100, and 120 µm. Consequently, the NiTi production run is made up of 12 families (named from F1 to F12), composed by 3 samples each (see Table 2). Along with the main process parameters, a set of secondary parameters associated to the borders was contextually defined (see Appendix B). This supplementary set of process parameters are specific of the used powder bed fusion machine and was defined in accordance with the experience perfected on other metallic materials.

The absolute density of the as-built NiTi specimens was measured by the Archimedean method through an analytical balance (Gibertini E50/S2); mean density was calculated over three measurements per sample and at least two samples per family were considered. The Vickers' hardness

(VH) measurements were carried out using a micro-hardness tester (Leitz Miniload 2) under 200 g load and 15 s indentation time; mean VH was calculated over ten measurements at different locations per sample.

Phase transformation temperatures of the NiTi alloys were investigated by differential scanning calorimetry (DSC, Q100 TA Instr.). Analyses were carried out with a heating/cooling rate of 10 °C/min in the [−120 to 150 °C] range over two cycles per sample. The identification of the characteristic temperatures was achieved by the tangent method. Phase transformation temperatures were also examined in solubilized samples to verify Ni loss during the process. Solubilization was done at 950 °C for 5 h (final water quench).

The microstructural analysis of the NiTi powder as well as of the printed specimens was carried out by an X-ray diffraction (XRD) analyzer (PANalytical X' PERT PRO instrument) at room temperature. Additionally, an Energy Dispersive X-ray Spectrometer (EDS, INCA ENERGY 200 Oxford Instr.) connected to a scanning electron microscope (SEM LEO 1430) was employed to analyze printed parts.

Mechanical response in quasi-static loading condition was evaluated by compression tests at fixed temperature and by strain recovery analysis at fixed stress. To avoid buckling during compression tests, the height of each bar has been reduced to 5 mm through a non-consumable diamond blade and the contacting surface were refined by means of metallographic grinding. Compression measurements were

Table 2 Matrix (4 rows, 3 columns) representing the twelve NiTi families

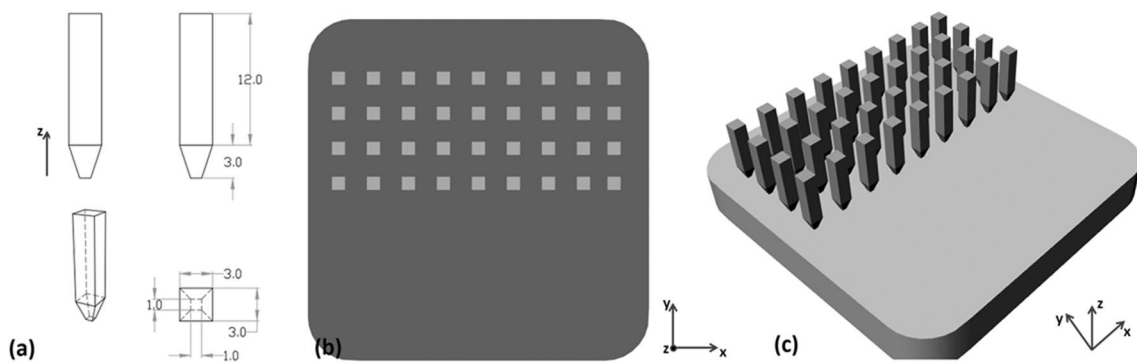|	$t = 60$ µs $v = 1000$ mm/s	$t = 48$ µs $v = 1250$ mm/s	$t = 40$ µs $v = 1500$ mm/s
h1 = 50 µm	F1	F2	F3
h2 = 75 µm	F4	F5	F6
h3 = 100 µm	F7	F8	F9
h4 = 120 µm	F10	F11	F12

Fig. 1 CAD model (dimensions in mm), (**a**), and sketches of the NiTi bar and of the production run, (**b**) and (**c**)

accomplished by an MTS 2/M machine (10 kN load cell) connected to an extensometer, at 0.5 mm/min crosshead rate and at Af + 10 °C (where Af is the austenite finish temperature resulting from DSC analysis). Five loading/unloading cycles at 4% strain were accomplished. Strain recovery was assessed in the three-point bending configuration in a Q800 (TA Instr.) device; homemade steel holders were fixed on to Q800 clamp to reduce the span length to less than 7 mm. Samples were prepared to have tape geometry with length of 12 mm, width of 3 mm and thickness lower than 0.4 mm. Strain recovery measurements were accomplished at 50, 100, 150, 200 and 250 MPa in the [− 70 to 150 °C] range with a heating/cooling rate of 5 °C/min.

Dynamic analyses were carried out with an Instron ElectroPuls E3000 instrument equipped with a thermal chamber. Samples were prepared to have the same geometry of quasi-static compression tests. Measurements were accomplished at Af + 10 °C temperature, at 4% strain for 10^3 loading/unloading cycles and at a solicitation frequency of 1 Hz.

Damping response in quasi-static and dynamic loading conditions was evaluated by the loss factor η [36], which is defined by the following equation:

$$\eta = \frac{W}{2 \cdot \pi \cdot W_{\text{loading}}} \tag{1}$$

where, W is the loss energy and it is the area between the loading and unloading curves, W_{load} is the mechanical energy stored during the loading path, and the W/W_{load} ratio is the specific damping capacity. Finally, the depth of the melt pools was estimated through ImageJ open source software from optical micrographs. In this analysis, microscope images (taken by a Leitz-ARISTOMET light optical microscope) have been used. For microscope observations, samples were embedded in epoxy resin and then mechanically grounded and polished up to 2500 grit papers, followed by surface refining with micrometric diamond powder (from 6 to 1 μm of powder dimension), and then chemically etched with 3%HF + 12%HNO3 + 85%H2O for 30 s (three separate steps of 10 s each).

3 Results

3.1 Powder characterization

The result of the DSC analysis of the supplied NiTi powder is reported in Fig. 2 and Table 3. The DSC trend is characterized by multi peaks that are reasonably due to inhomogeneity, i.e., local change in composition and crystalline size [23]. Table 3 reports the phase transformation temperatures and the transformation enthalpies of the NiTi powder before and after the production run. After the first production run, the
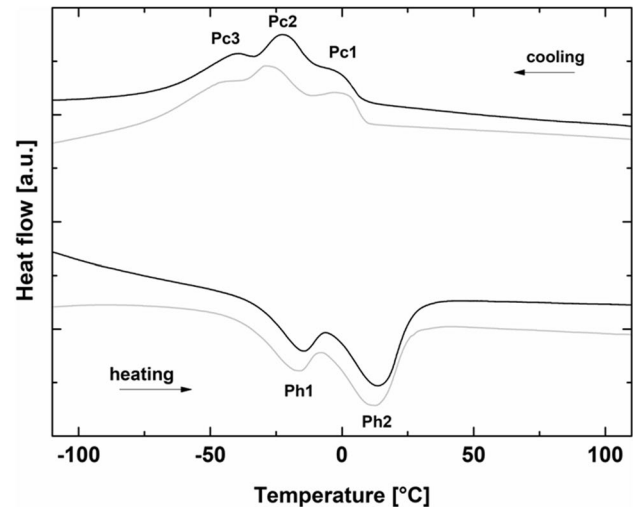
Fig. 2 DSC of the provided NiTi micrometric powder before (black line) and after (grey line) the first production run

NiTi powder presents thermal properties similar to that of the feedstock; negligible fluctuations of few degrees centigrade were observed for the phase transformation temperatures.

3.2 Density and micro-hardness

Figure 3 shows a photograph of the NiTi production run; NiTi parts are grouped in a 4 × 3 matrix where each element represents a family of process parameters. The laser energy density (J/mm³) related to the 12 NiTi families is reported in Table 4. It can be noticed that there are two couples of NiTi elements, in the position (1;3), (2;1) (i.e., families F3 and F4) and (3;3), (4;2) (i.e., families F9 and F11), with the same laser energy density, 111.1 J/mm³ and 55.6 J/mm³, but with different h and v parameters.

Figure 4 reports the density percentage and Vickers' hardness data as a function of the laser energy density. For each family, the density percentage was calculated as the ratio between the measured absolute density and the density of the NiTi as bulk (6.45 g/cm³ [37]). Results confirm that the set of process parameters selected in this study is appropriate as the most specimens are near fully dense alloys with density higher than 99% (for comparison, Appendix A reports an optical microscope observation); furthermore, the density is almost constant with the increasing of the laser energy, except for F1 family for which density is lower. Major details are reported in the density maps of Fig. 5 where it can be seen a broad area in which density is maximized. In contrast, micro-hardness is rather dependent by the process parameters, clearly indicating the effect on mechanical performances depending on the resulting material microstructure after the selective laser melting production. An absolute minimum is visible near 80 J/mm³,

Table 3 Phase transformation temperatures of the NiTi powder before and after the first production run

	Cooling						Heating				
	Ms [°C]	P_c1 [°C]	P_c2 [°C]	Pc3 [°C]	Mf [°C]	ΔH_c [J/g]	As [°C]	P_h1 [°C]	P_h2 [°C]	Af [°C]	ΔH_h [J/g]
Feedstock	10	− 5	− 22.3	− 39.2	− 68.5	15.3	− 34.5	− 14.7	13.4	28.2	15.4
After first production run	9.8	− 3	− 29.5	− 39.5	− 72.5	21.4	− 42.8	− 16	12.5	26	17.52
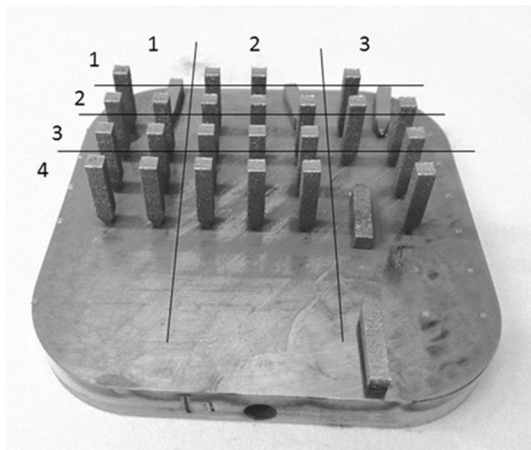
Fig. 3 Photograph of the NiTi production run; the different quadrants identified the 12 sample families obtained through different processing parameters

which corresponds to a low scanning speed (1000 mm/s) and 100 μm hatching distance (F7 family), see the map of Fig. 5. Besides, it was observed that the micro-hardness is high when the parameters (hatching distance and scanning speed) are $h = 50$ μm and $v = 1000$ mm/s (F1 family) and $h = 120$ μm and $v = 1500$ mm/s (F12 family).

3.3 Microstructure and thermal properties

Figure 6a, b reports the phase transformation temperatures of the 12 as-built NiTi families (As, Af, Ms and Mf are the start and finish temperature of austenite, A, and martensite,

M, respectively). Results show that all the printed parts have Af higher than that of the provided NiTi powder (see Table 3) and out of the pseudoelasticity field (that was assumed below 25 °C). Hence, from DSC data, it can be established that a microstructural change occurs through the laser beam melting process since the NiTi material lost the pseudoelastic property [1]. Furthermore, the 12 combinations of the process parameters generate 12 different NiTi families each of them with specific phase transformation temperatures. No particular trend with the laser energy is observed; the lowest Af is at $h = 100$ μm and $v = 1000$ mm/s (F7 family), and the highest Af is observed at $h = 100$ μm and $v = 1500$ mm/s (F9 family), see the graph and the map of Fig. 6c, d. A microstructural change is confirmed by XRD spectra taken at room temperature: in Fig. 7, it can be seen that the feedstock powder is in the austenitic phase while the 12 families show some minor peaks representing the B19′ martensite phase, superposing those of the austenite.

Figure 8 depicts the phase transformation temperatures of the 12 NiTi families after solubilization at 950 °C. The applied thermal treatment slightly homogenizes the transformation temperature for all families (Fig. 8a, b). Narrowing of transition peaks is also detected, indicating a more homogeneity in the material composition (see Appendix E). Furthermore, all samples still present phase transformation temperatures higher than those of the NiTi powder.

3.4 Mechanical and functional responses

In the austenite phase, samples of all families show the characteristic hysteretic pseudoelastic behavior; Fig. 9 reports

Table 4 Laser energy densities [J/mm³] of the twelve NiTi families

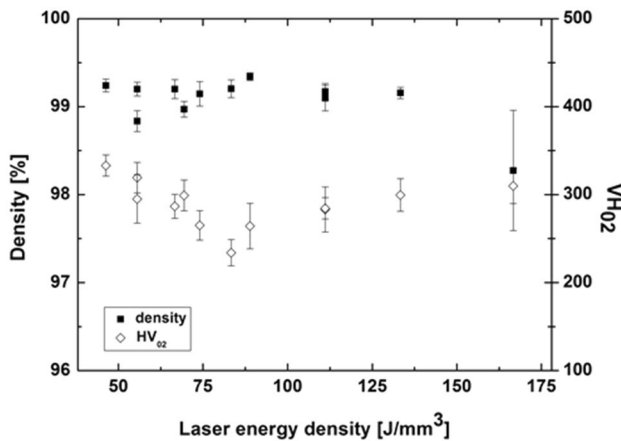|	1	2	3
1	166.7 (F1: $h = 50$ μm; $v = 1000$ mm/s)	133.3 (F2: $h = 50$ μm; $v = 1250$ mm/s)	111.1 (F3: $h = 50$ μm; $v = 1500$ mm/s)
2	111.1 (F4: $h = 75$ μm; $v = 1000$ mm/s)	88.9 (F5: $h = 75$ μm; $v = 1250$ mm/s)	74.1 (F6: $h = 75$ μm; $v = 1500$ mm/s)
3	83.3 (F7: $h = 100$ μm; $v = 1000$ mm/s)	66.7 (F8: $h = 100$ μm; $v = 1250$ mm/s)	55.6 (F9: $h = 100$ μm; $v = 1500$ mm/s)
4	69.4 (F10: $h = 120$ μm; $v = 1000$ mm/s)	55.6 (F11: $h = 120$ μm; $v = 1250$ mm/s)	46.3 (F12: $h = 120$ μm; $v = 1500$ mm/s)

Fig. 4 Density percentage and micro-hardness of the 12 NiTi families as a function of the laser energy density

the compression curves registered at Af + 10 °C of a representative as-built sample of F6 family (compression curves of all the families are reported in Appendix C). Different mechanical responses have been observed between samples; the main mechanical outcomes are collected in the graphs of Fig. 10, which represent the residual strain and the maximum stress as a function of the mechanical cycle and in the map of Fig. 11 where the austenite elastic modulus (E_A) and the loss factor as a function of the process parameters are reported. Firstly, in Fig. 10, a gradual stabilization with cycling is observable: in the first cycle there is the highest residual deformation (sample of F12 family has the highest permanent deformation after the first mechanical cycle). At the fifth loading–unloading cycle, all samples present an almost stable mechanical response (see also Appendix C). The maximum stress slightly increases with mechanical cyclic; the maximum stress is achieved by the samples of F2 and F9

families. Austenite elastic modulus, E_A, was evaluated in the first cycle between 100 and 200 MPa. It was found that E_A does not change significantly with process parameters (see Fig. 11a): the highest modulus (near 60 GPa) has been observed with $h = 75$ μm and $v = 1000$ mm/s (sample of F4 family); the austenite elastic modulus of the other specimens is near 40 GPa. Sample of F1 family present the lowest E_A. Figure 11b reports the loss factor calculated through the pseudoelastic curves of the quasi-static tests. It can be noticed that the sample with the highest damping property is the one obtained with $h = 120$ μm, $v = 1250$ mm/s (F11 family). Figure 12 depicts the elastic modulus and loss factor as a function of the laser energy density; it can be seen that both of them do not show noticeable variations with respect to the laser energy, except at high laser energy density, where the elastic modulus presents an anomalous value.

In dynamic condition, the flag-shaped pseudoelastic curve is hindered. As an example, Fig. 13 depicts a representative dynamic response at the first, at the second and at the 1000th cycles. Furthermore, Fig. 14 shows that at 1 Hz and in stabilized condition (1000th cycle), the loss factor is near one order of magnitude lower than that registered in quasi-static condition. It can be noticed a diagonal area from left to right in the map of process parameters with high loss factor values. The sample with the highest loss factor is the one obtained with $h = 100$ μm and $v = 1000$ mm/s (F7 family).

A representative example of functional response by strain recovery analysis of NiTi as-built sample is reported in Fig. 15 where the strain recovery of a sample of F9 family is represented (strain recovery curves of all the families are reported in Appendix D). The trend of the maximum strain and the thermal hysteresis as a function of the applied stress during the stain recovery tests are displayed in the two graphs of Fig. 16. It can be noticed the specimens of F4 and F12 families have the highest recovered stroke; F12
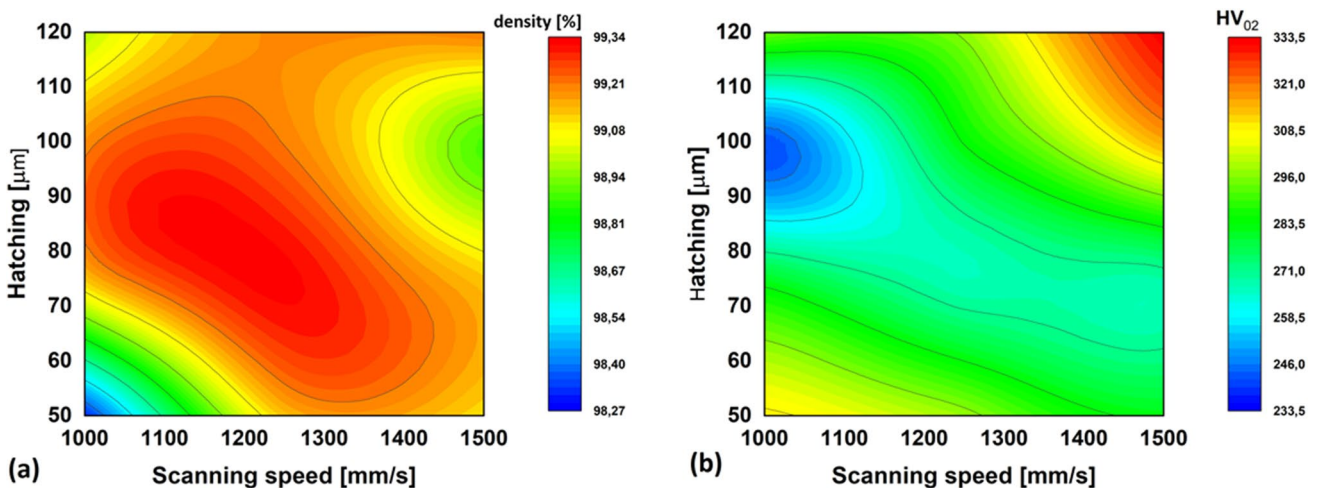

Fig. 5 Density percentage (**a**) and micro-hardness (**b**) maps as a function of hatching distance and scanning speed parameters
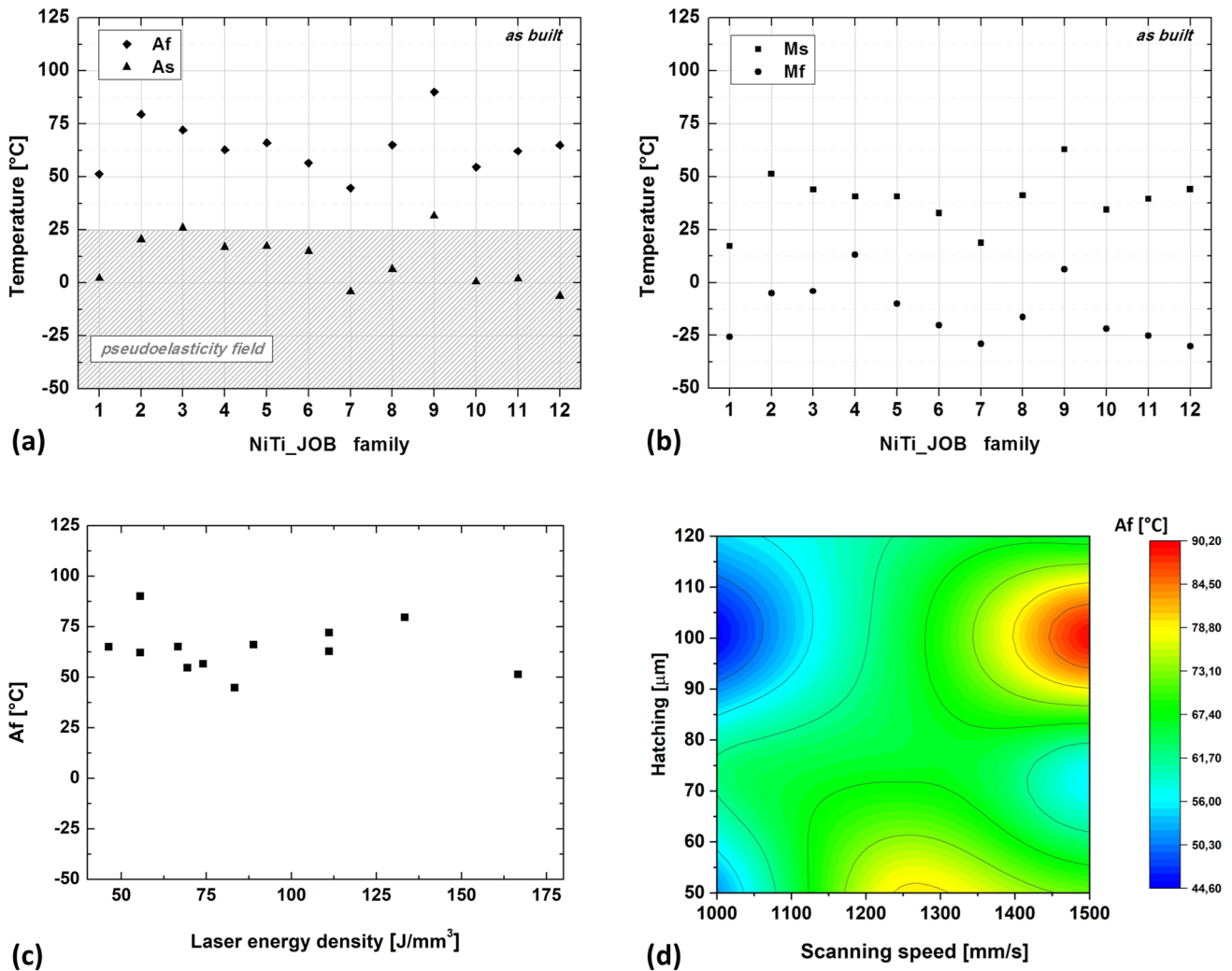
Fig. 6 a, **b** Phase transformation temperatures of the 12 families of the NiTi as-built samples (As, Af, Ms and Mf are the start and finish temperature of austenite, A, and martensite, M). **c** Af temperature as a function of the laser energy. **d** Af temperature as a function of the hatching and scanning speed parameters

sample also exhibits the highest thermal hysteresis. The worst response has been registered on sample of F1 family.

Finally, Fig. 17a, b depict the estimated melt pool depths as a function of the hatching distance and the laser energy density, respectively. It is possible to observe that high melt pool depths are obtained at low hatch distance and at high laser energy density.

4 Discussion

The first outcome concerns the change of the phase transformation temperatures of the as-built specimens with respect to the provided feedstock NiTi powder. The Af of the NiTi powder is 28.5 °C; it means that the powder is classified as a near body-temperature alloy whose applications are mainly

found in the biomedical field [5]. Nevertheless, these alloys are defined as pseudoelastic materials due to the excess of Ni. In this work, the Af of the selective laser melted products is higher than the feedstock independently from the process parameters. According to DSC data, it was found that Af varies from 45 to 90 °C while Mf changes from − 25 to − 13 °C. Furthermore, no relationship with laser energy density was found. The first reason of the increasing of transition temperatures with respect to those of the powder may be ascribed to the evaporation of Ni during the process (55.2 wt.% Ni content in the feedstock powder). This is confirmed by EDX analysis; as examples, Ni content of F2 and F3 families is 54.63 wt.% (0.32 st. dev.) and 55.13 wt.% (0.01 st. dev.), respectively. Precipitate formation may also contribute in some extent to this effect [26]. Dissolution of precipitates and microstructure homogenization
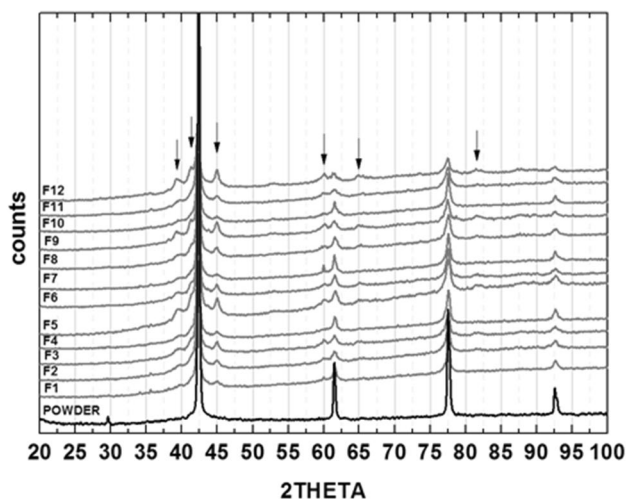
Fig. 7 XRD spectra of the 12 NiTi families at room temperature (arrows pointed the martensite B19′ XRD peaks)

may be achieved through solubilization at high temperature. After solubilization, NiTi parts still present Af higher than that of the feedstock powder confirming that Ni loss occurs during the process. As observable in the graph of Fig. 8c, Af presents a trend with a maximum at 120 J/mm³. Considering the single process parameters (Fig. 8d), it can be said that after solubilization, the lowest Af is at $h = 120$ μm and $v = 1000$ mm/s (F10 family) which is different as the one of the as-built condition; on the contrary, the highest Af is still at $h = 100$ μm and $v = 1500$ mm/s (F9 family).

Solubilization heat treatment was employed to confirm the Ni loss during the process. Besides, further considerations may be derived from the as-built specimens. It is known that precipitates arise with aging [1]; in the presented work, the formation of precipitates is thought to be principally enhanced by the pulsed wave emission laser source, which generates additional regions where aging occurs. These regions derives from the overlapping of two consecutive laser spots (pulse overlap). The pulse overlap occurs only for pulse wave emission lasers [34] and it principally depends on the point distance d and on the exposure time t parameters. Since d was kept constant in the present study, pulse overlap was mainly ascribed to t parameter. Furthermore, precipitation is also pronounced for lower h values since the band of overlaying of adjacent laser tracks (line overlap) increases with the decreasing of h. Besides, melt pool depth may also increase the regions where material re-melts; re-melting causes further aging on the near-by material. Considering the as-built specimens, it was found that melt pool depth with low h is larger, as presented in Fig. 17a. Additionally, the melt pool depth increases with the laser energy density (Fig. 17b). These observations indicate that high h and low laser energy density have to be considered to avoid aging and the subsequent

formation of precipitates, which affects the Ni–Ti ratio in the material and promotes a coherent change of the material properties. As an example, Fig. 18 depicts the micro-hardness of the 12 families as a function of the respective Af temperature, it can be concluded that micro-hardness increases with Af temperature. Since Af increases with the decreasing of Ni in the matrix, it can be stated that precipitates and Ni loss may also contribute to the increasing of micro-hardness. It is worth underlining that the expected melt pool geometry is strongly affected by the emission mode of the laser. In general, for continuous wave emission mode, the laser energy cannot be the absolute factor to determine the melt pool dimension. Despite the same energy density, the melt pool formation can be different depending on the examined laser process parameters as well as the profile of the laser beam. In case of a pulse wave mode, rapid cooling rate and higher curvatures of melt pools are registered, resulting in finer columnar dendrite structures with relative high tilting angle [34].

A further experimental evidence that is worth to highlight, is the effect of h and v with respect to the laser energy on the thermo-mechanical properties. Families with identical laser energy (F3 and F4; F9 and F11) but different h and v parameters were studied. These couples of samples, in spite of same laser energy density, have different mechanical and thermal responses. Table 5 summarized the main characteristics of these samples.

Data of Table 5 clearly indicate that the laser energy density can only be used as a preliminary guidance since it is not sufficient for a full control of the overall performance of NiTi parts produced by selective laser melting even though it summarizes several active process parameters. It was found that each (h, v) couple plays a predominant role in determining a specific set of phase transformation temperatures and consequently a precise mechanical and functional responses. With this regard, samples of each family may be considered as a pseudoelastic or as a shape memory material. In the austenite field, quasi-static compression tests show well-defined pseudoelastic curves. In this condition, good damping performance are exhibited by samples of F2 ($h = 50$ μm, $v = 1250$ mm/s) and F11 ($h = 120$ μm, $v = 12,500$ mm/s). In dynamic condition, the mechanical curve loses the flag shape and the highest loss factors is exhibited by samples of F6 ($h = 75$ μm, $v = 1500$ mm/s) and F7 ($h = 100$ μm, $v = 1000$ mm/s) families.

As concerns the shape memory effect, high strain recoveries at different stress levels and low residual strains have been registered in quasi-static thermal cycles. In this regard, the choice of $h = 75$ μm and $v = 1000$ mm/s (F4 family) and $h = 120$ μm and $v = 1500$ mm/s (F12 family) produces promising shape memory performance. Finally, in both the quasi-static mechanical studies (compression and strain recovery tests) as well as density measurements, the choice of $h = 50$ μm and $v = 1000$ mm/s (which correspond to F1 family) has brought the worst outcomes.
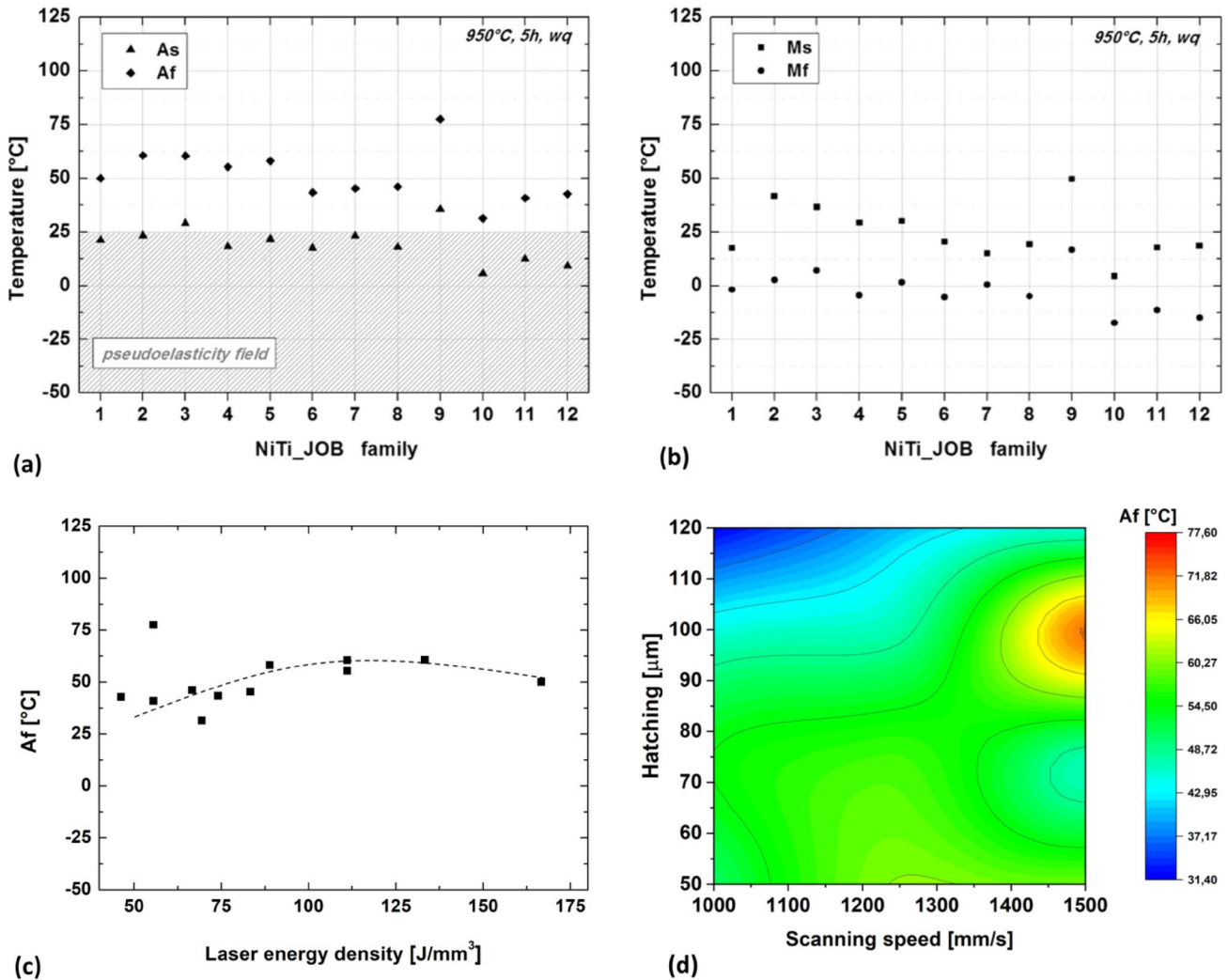
Fig. 8 Effect of solubilization: (**a**) and (**b**): phase transformation temperatures of the 12 families; (**c**): Af temperature as a function of the laser energy; Af as a function of the hatching and scanning speed parameters (**d**)
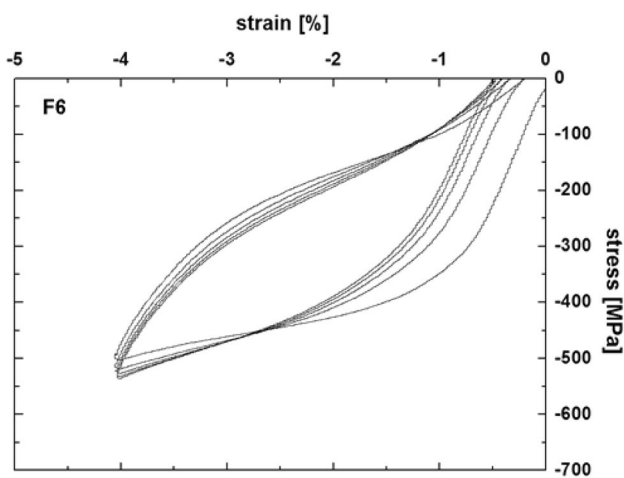

Fig. 9 Compression tests of the as-built sample of F6 family

5 Conclusions

In this work, Ni-rich NiTi powder was used to fabricate several NiTi components by selective laser melting. Findings were collected to show the functional and mechanical properties of the specimens and the effect of h and v process parameters compared to those associated to the laser energy density. Two fundamental outcomes were obtained:

1. A loss of Ni was observed on the as-built parts. This caused an increase of the phase transformation temperatures of the printed parts (with Af that varies from 45 to 90 °C) with respect to the powder (Af = 28.5 °C). Consequently, all as-built samples performed the shape memory property at room temperature.

2. Process parameters h and v resulted to be more effective than the laser energy density in defining the mechanical performance. In particular, two couples of (h, v) parameters
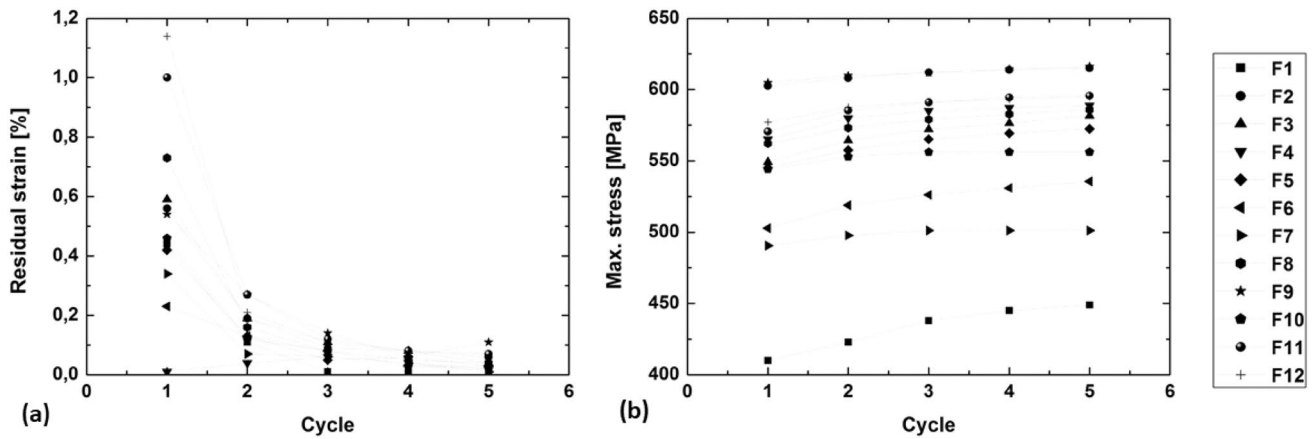
Fig. 10 Residual strain (**a**) and maximum stress (**b**) of the 12 NiTi families as a function of the mechanical cycle
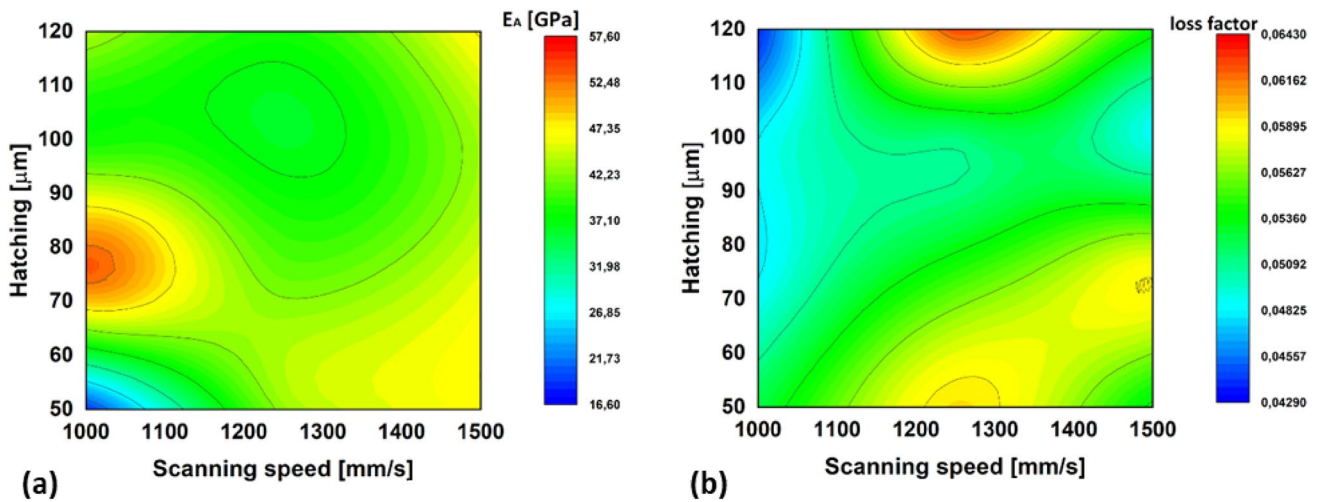
Fig. 11 a austenite elastic modulus [GPa] in compression quasi-static tests, as a function of the of hatching distance and scanning speed parameters. **b** Loss factor map as a function of the hatching and scanning speed parameters at 5th cycle of quasi-static compression tests
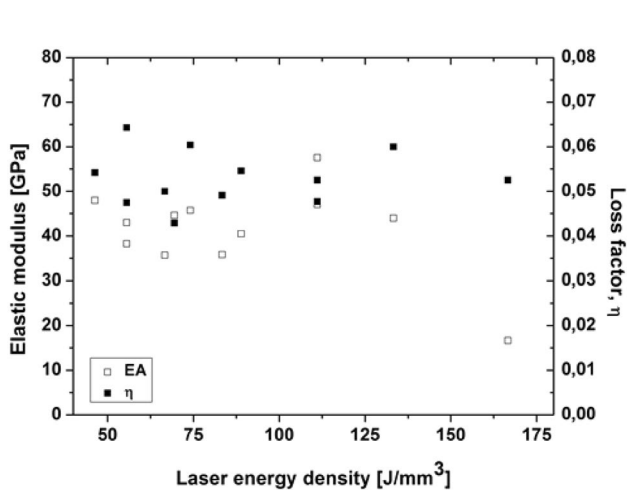

Fig. 12 Elastic modulus and loss factor as a function of the laser energy density related to quasi-static compression tests
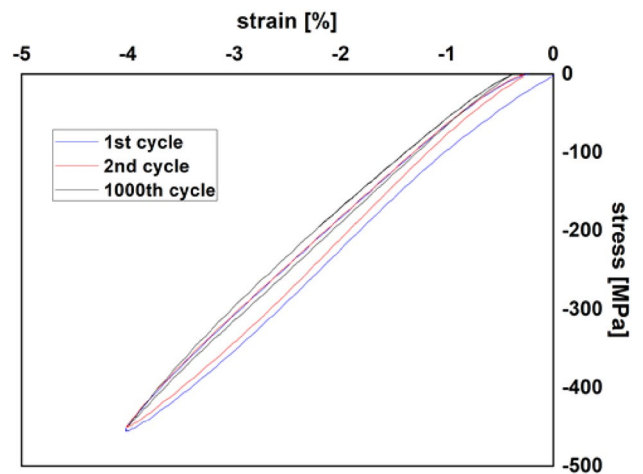
Fig. 13 Dynamic response of sample of F7 family (1st, 2nd and 1000th cycle, 4% strain and 1 Hz of solicitation frequency)
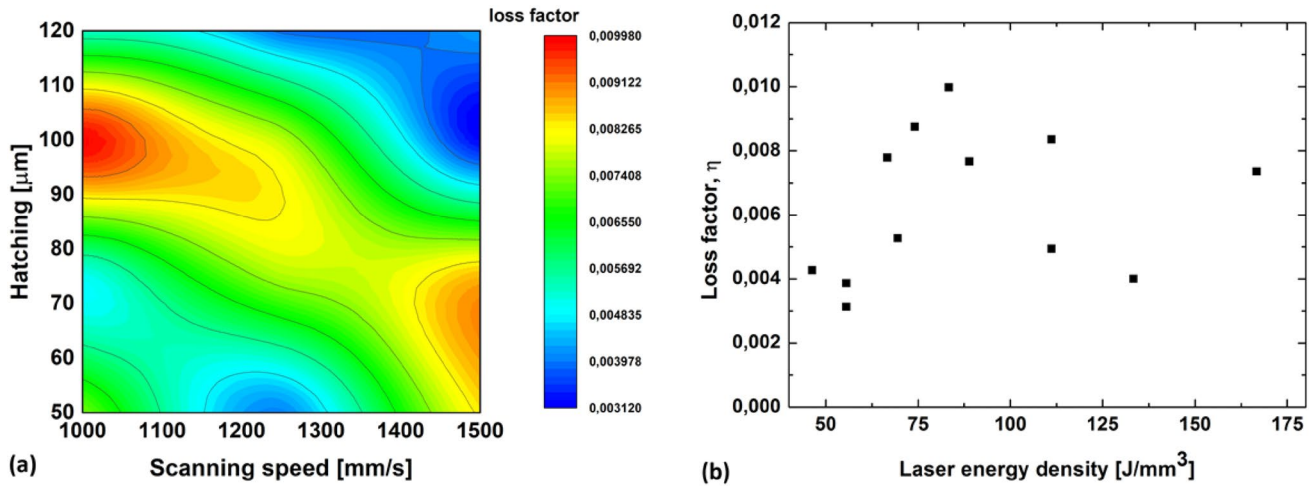
Fig. 14 Loss factor maps as a function of the hatching and scanning speed parameters, (**a**), and as a function of the laser energy density, (**b**), at 1000th cycle, 4% strain and 1 Hz of solicitation frequency
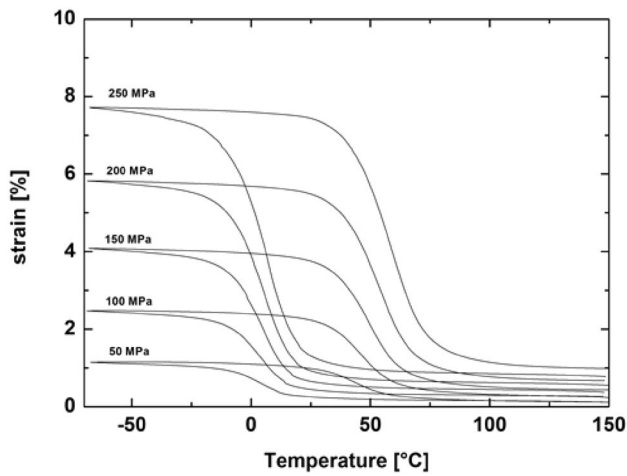

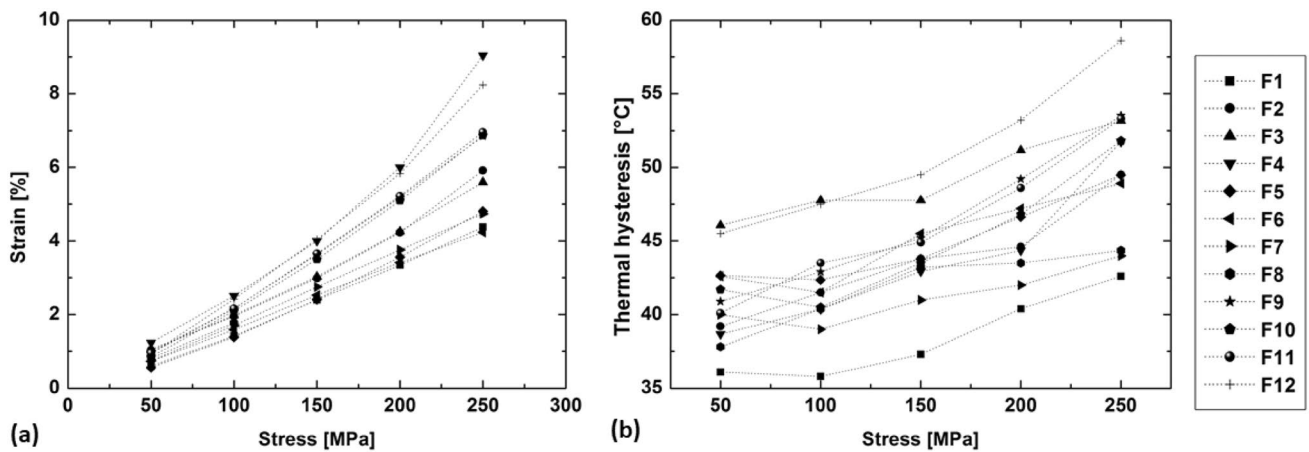**Fig. 15** Strain recovery tests of sample of F9 family

assure an increased dynamic damping response: (75 μm, 1500 mm/s) and (100 μm, 1000 mm/s). Besides, the shape memory response is maximized when parameters are (75 μm, 1000 mm/s) and (120 μm, 1500 mm/s).

Finally, in this work, no observations taken at different locations of the sample are reported. In particular, the mechanical response was observed considering the whole sample. It is worth to point out that different locations may present a specific microstructure due to different cooling speeds. To this end, since NiTi alloys are very responsive to a change of microstructure, it is recommended to evaluate the effect of the geometry on the homogeneity of measurements in case of more complex NiTi structures.
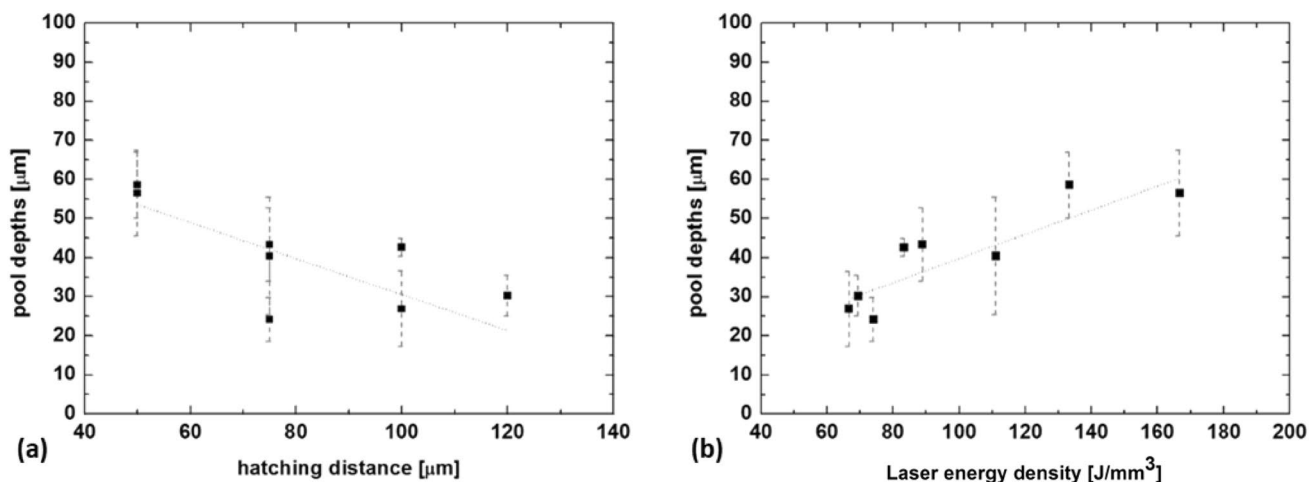

Fig. 16 Maximum strain (**a**) and thermal hysteresis (**b**) of the 12 NiTi families as a function of the applied stress

Fig. 17 Estimated depths of the melt pools as a function of the hatching distance (**a**) and of the laser energy density (**b**)
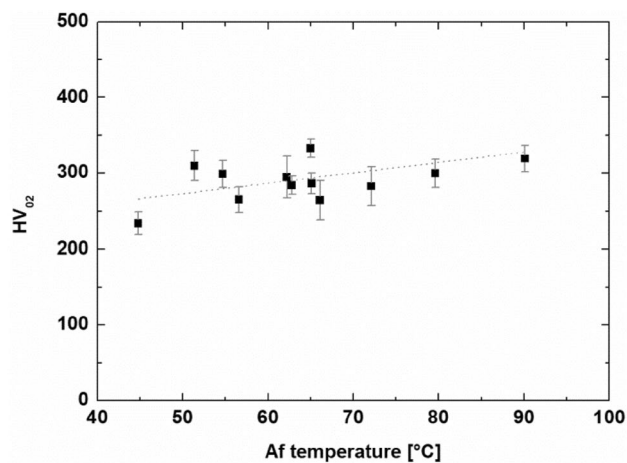

Fig. 18 Micro-hardness as a function of the Af temperature of the 12 as-built NiTi families

6 Conflicts of interest

On behalf of all authors, the corresponding author states that there is no conflict of interest.

Table 5 Main characteristics of as-built samples of F3, F4, F9 and F11 families

	F3 $E=111.1$ J/mm^3 $h=50$ μm; $v=1500$ mm/s	F4 $E=111.1$ J/mm^3 $h=75$ μm; $v=1000$ mm/s	F9 $E=55.6$ J/mm^3 $h=100$ μm; $v=1500$ mm/s	F11 $E=55.6$ J/mm^3 $h=120$ μm; $v=1250$ mm/s
Density [%]	99.096 ± 0.145	99.172 ± 0.091	98.835 ± 0.119	99.199 ± 0.079
Af [°C]	70	63	90	61
HV$_{02}$	283 ± 25	284 ± 12	327 ± 17	290 ± 27
E_A [GPa]	47.1	57.5	43	38.3
σ_{max} [MPa]	582	589	616	596
Recovered ε [%]	5.5	9	6.8	7
Static η	0.0525	0.0477	0.0475	0.0643
Dynamic η	0.00836	0.00494	0.00313	0.00387

Appendix A: SEM and optical microscope observations
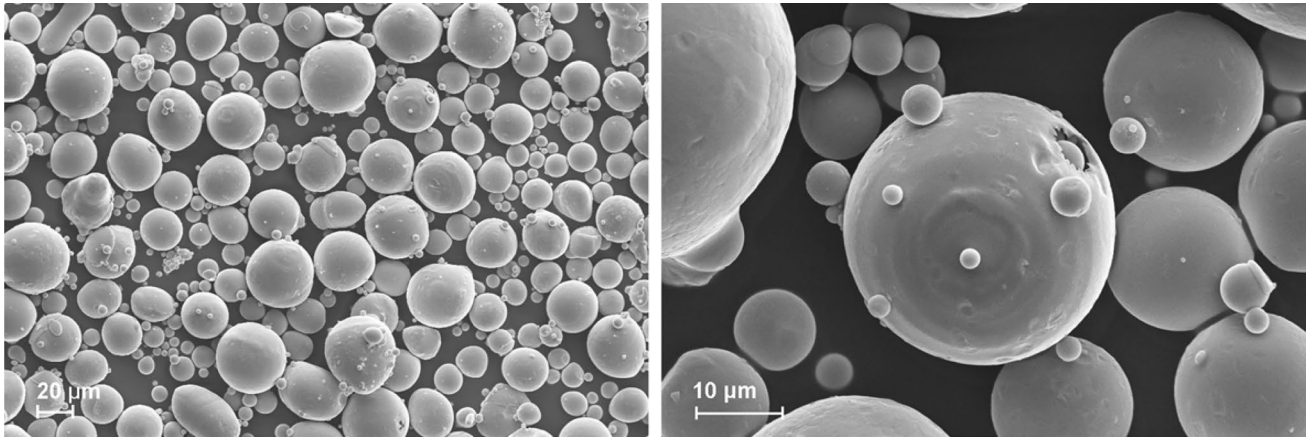
See appendix Figs. 19, 20.
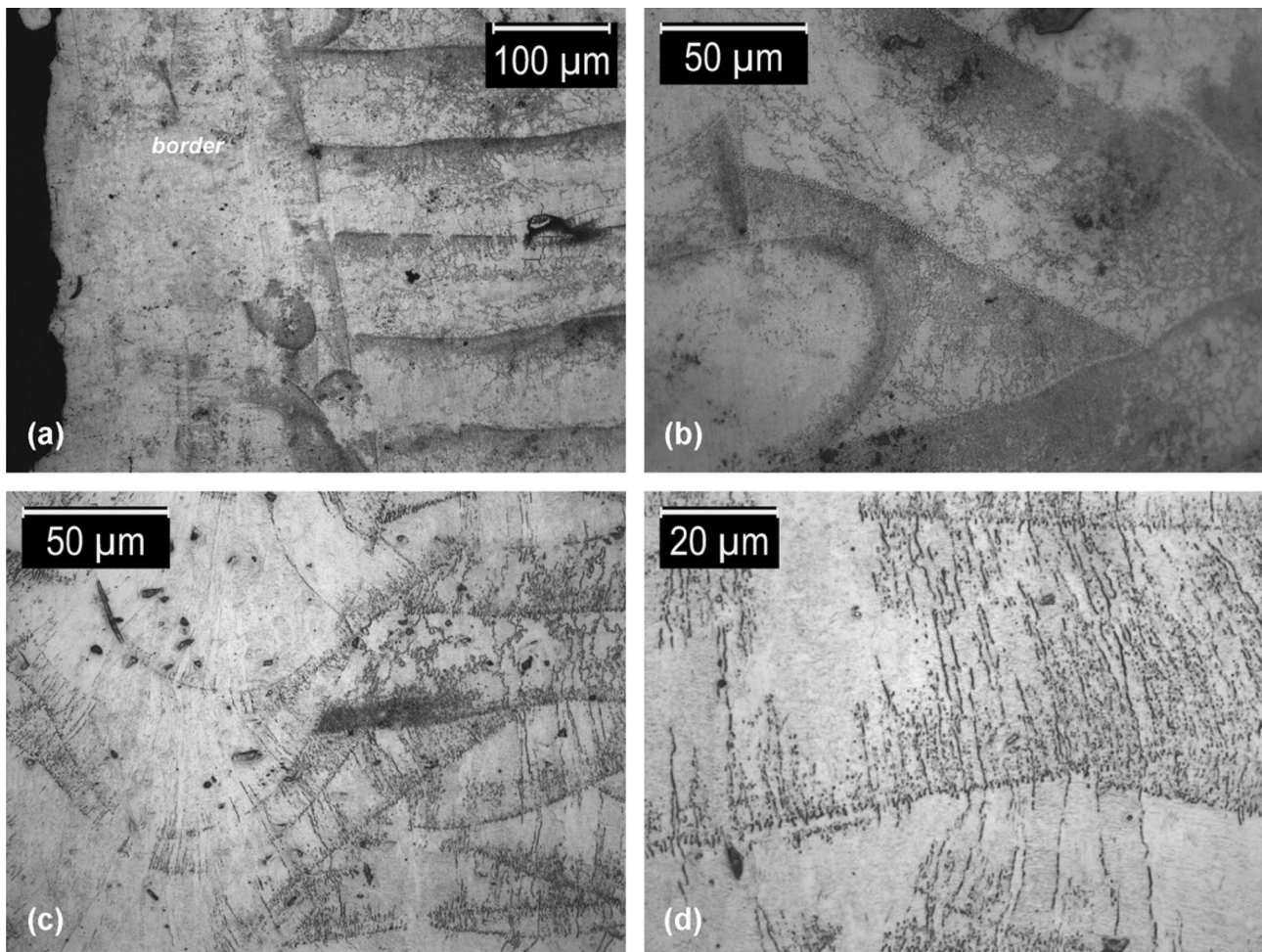

Fig. 19 SEM observation of the NiTi powder

Fig. 20 Optical microscope images at two magnifications of representative as-built samples of F2 family perpendicular to the building direction (**a** and **b**) and of F7 family along building direction (**c** and **d**)

Appendix B: Process parameters for borders

| Beam compensation	0.1 mm
Number of borders	2
Border distance	0.1 mm
Border power	125 W
Border exposure time	55 μs
Border point distance	40 μm
Border focus	0

Appendix C: Compression tests of all families in as-built condition
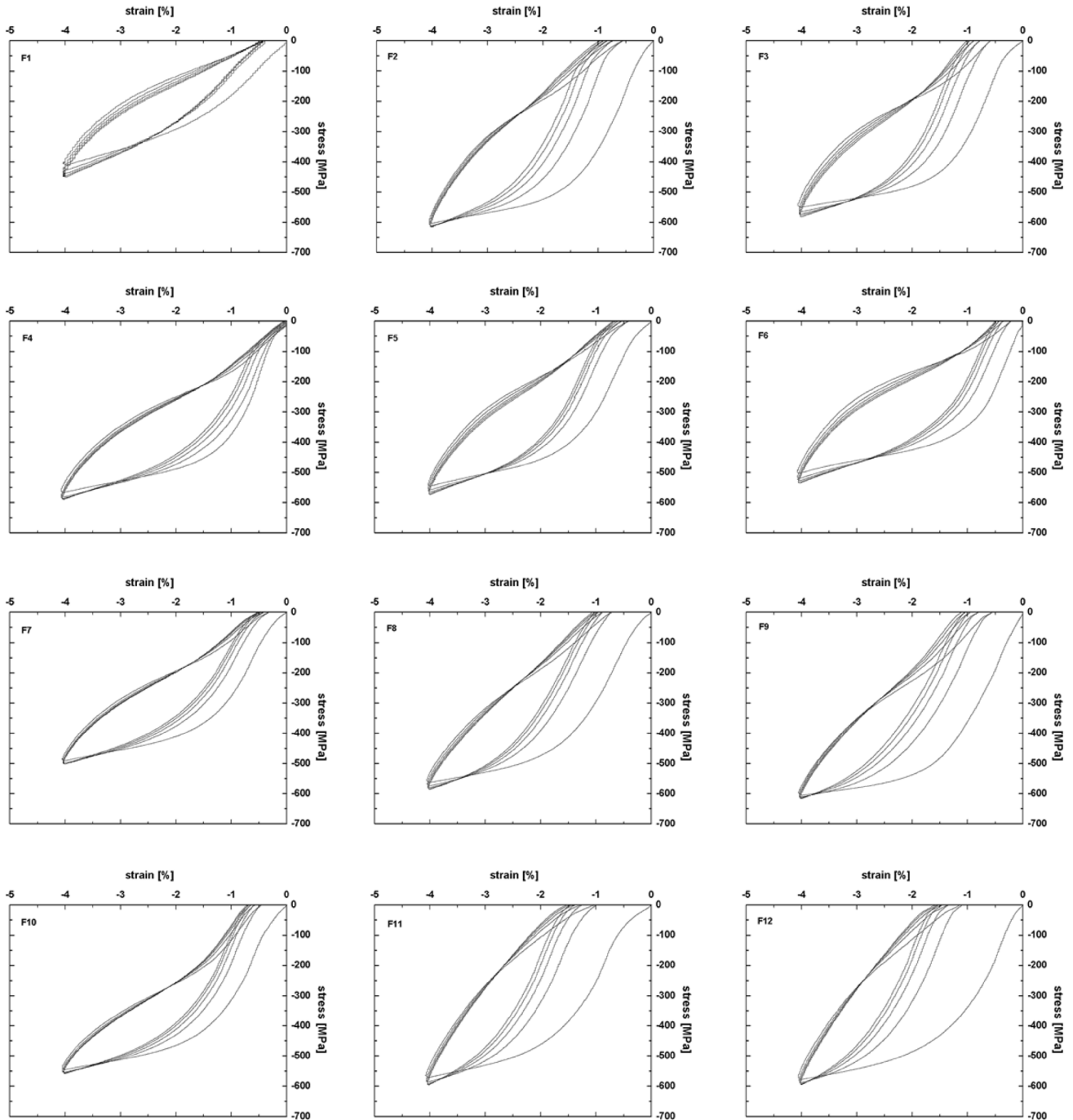
Appendix D: Strain recovery tests of all families in as-built condition
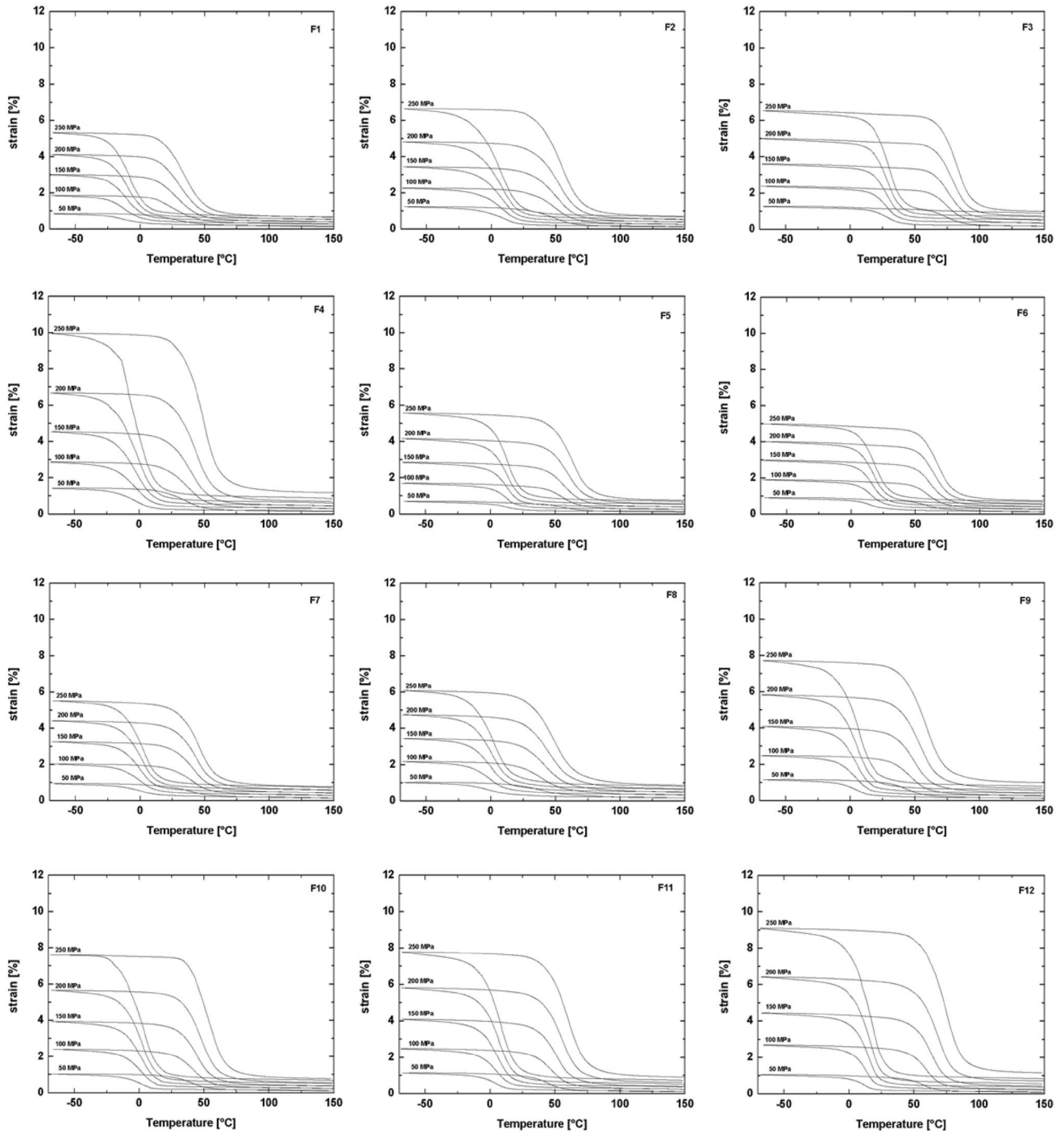
Appendix E: Extend of the austenite and martensite peak in as-built and solubilized conditions
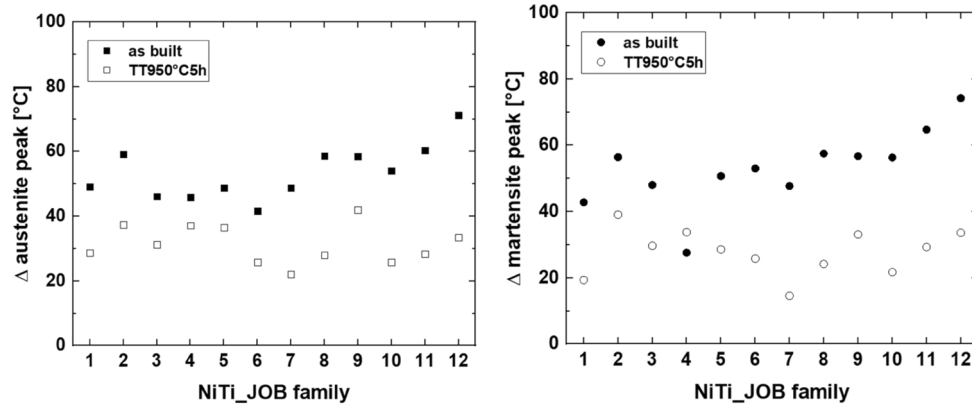
References

1. Otsuka K, Ren X (2005) Physical metallurgy of Ti–Ni-based shape memory alloys. Progress Mater Sci 50:511–678. https://doi.org/10.1016/j.pmatsci.2004.10.001

2. Pons JL (2005) Emerging actuator technologies: a micrometric approach. Wiley, New York

3. Nespoli A, Besseghini S, Pittaccio S, Villa E, Viscuso S (2010) The high potential of shape memory alloys in developing miniature mechanical devices: a review on shape memory alloy mini-actuators. Sens Actuators A Phys 158:149–160. https://doi.org/10.1016/j.sna.2009.12.020

4. Hartl DJ, Lagoudas DC (2007) Aerospace applications of shape memory alloys. Proc IMechE Part G J Aero 221(4):535–552. https://doi.org/10.1243/09544100JAERO211

5. Petrini L, Migliavacca F (2011) Biomedical Applications of Shape Memory Alloys. J Metal 1-15. https://doi.org/10.1155/2011/501483

6. Jani JM, Leary M, Subic A, Gibson MA (2014) A review of shape memory alloy research, applications and opportunities. Mater Des 56:1078–1113. https://doi.org/10.1016/j.matdes.2013.11.084

7. Kaynak Y, Tobe H, Noebe RD, Karaca HE, Jawahir S (2014) The effects of machining on the microstructure and transformation behavior of NiTi Alloy. Scripta Mater 74:60–63. https://doi.org/10.1016/j.scriptamat.2013.10.023

8. Wu SK, Lin HC, Chen CC (1999) A study on the machinability of a Ti49.6Ni50.4 shape memory alloy. Mater Lett 40:27–32. https://doi.org/10.1016/S0167-577X(99)00044-0

9. Wang G, Liu Z, Huang W, Wang B, Niu J (2019) Influence of cutting parameters on surface roughness and strain hardening during milling NiTi shape memory alloy. Int J Adv Manuf Technol 102:2211–2221. https://doi.org/10.1007/s00170-019-03342-9

10. Mehta K, Gupta K (2019) Machining of Shape Memory Alloys. In: Fabrication and Processing of Shape Memory Alloys. Springer Briefs in Applied Sciences and Technology. Springer, Cham

11. Nespoli A, Rigamonti D, Villa E, Passaretti F (2014) Design, characterization and perspective of shape memory alloy elements in miniature sensor proof of concept. Sens Actutors A Phys 218:142–153. https://doi.org/10.1016/j.sna.2014.08.001

12. Nespoli A, Rigamonti D, Riva M, Villa E, Passaretti F (2016) Study of pseudoelastic systems for the design of complex passive dampers: static analysis and modeling. Smart Mater Struct 25:105001. https://doi.org/10.1088/0964-1726/25/10/105001

13. Nespoli A, Dallolio V, Villa E, Passaretti F (2015) A new design of a Nitinol ring-like wire for suturing in deep surgical field. Mater Sci Eng C 56:30–36. https://doi.org/10.1016/j.msec.2015.06.009

14. Herzog D, Seyda V, Wycisk E, Emmelmann C (2016) Additive manufacturing of metals. Acta Mater 117:371–392. https://doi.org/10.1016/j.actamat.2016.07.019

15. Yadroitsev I, Smurov I (2010) Selective laser melting technology: from the single laser melted track stability to 3D parts of complex shape. Phys Procedia 5:551–560. https://doi.org/10.1016/j.phpro.2010.08.083

16. Liverani E, Fortunato A, Leardini A, Belvedere C, Siegler S, Ceschini L, Ascari A (2016) Fabrication of Co–Cr–Mo endoprosthetic ankle devices by means of selective laser melting (SLM). Mater Des 106:60–68. https://doi.org/10.1016/j.matdes.2016.05.083

17. Mullen L, Stamp RC, Brooks WK, Jones E, Sutcliffe CJ (2008) Selective laser melting: a regular unit cell approach for the manufacture of porous, titanium, bone in-growth constructs, suitable for orthopedic applications. J Biome Mater Res 89B:275–576. https://doi.org/10.1002/jbm.b.31219

18. Elahinia MH, Hashemi M, Tabesh M, Bhaduri SB (2012) Manufacturing and processing of NiTi implants: a review. Prog Mater Sci 57:911–946. https://doi.org/10.1016/j.pmatsci.2011.11.001

19. Seabra M, Azevedo J, Araújo A, Reis L, Pinto E, Alves N, Santos R, Mortágua JP (2016) Selective laser melting (SLM) and topology optimization for lighter aerospace components. Proc Struct Integr 1:289–296. https://doi.org/10.1016/j.prostr.2016.02.039

20. Yadroitsev I, Krakhmalev P, YadroitsavaI, (2014) Selective laser melting of Ti6Al4V alloy for biomedical applications: temperature monitoring and microstructural evolution. J Alloys Comp 583:404–409. https://doi.org/10.1016/j.jallcom.2013.08.183

21. Walker JM, Haberland C, Andani MT, Karaca HE, Dean D, Elahinia M (2016) Process development and characterization of additively manufactured nickel-titanium shape memory parts. J Intell Mater Struct 27(19):2653–2660. https://doi.org/10.1177/1045389X16635848

22. Haberland C, Elahinia M, Walker JM, Meier H, Frenzel J (2014) On the development of high quality NiTi shape memory and

23. Dadbakhsh S, Speirs M, Kruth JP, Schrooten J, Luyten J, Van Humbeeck J (2014) Effect of SLM parameters on transformation temperatures of shape memory alloys Nickel Titanium parts. Adv Eng Mater 16(9):1140–1146. https://doi.org/10.1002/adem.20130 0558

24. Moghaddam NS, Saedi S, Amerinatanzi A, Hinojos A, Ramazzani A, Kudin J, Mills MJ, Karaca H, Elahinia M (2019) Achieving superelasticity in additively manufactured NiTi in compression without post-process heat treatment. Sci Rep 9:41. https://doi.org/10.1038/s41598-018-36641-4

25. Speirs M, Wang X, Van Baelen S, Ahadi A, Dadbakhsh S, Kruth JP, Van Humbeeck J (2016) On the transformation behavior of NiTi shape-memory alloy produced by SLM. Shape Memory Superelasticity 2:310–316. https://doi.org/10.1007/s40830-016-0083-y

26. Wang X, Kustov S, Van Humbeeck J (2018) A short review on the microstructure, transformation behavior and functional properties of NiTi shape memory alloys fabricated by selective laser melting. Mater 11:1683. https://doi.org/10.3390/ma11091683

27. Saedi S, Turabi AS, Andani MT, Haberland C, Elahinia M, Karaca H (2016) Thermomechanical characterization of Ni-rich NiTi fabricated by selective laser melting. Smart Mater Struct 25:035005. https://doi.org/10.1088/0964-1726/25/3/035005

28. Saedi S, Turabi AS, Andani MT, Haberland C, Karaca H, Elahinia M (2016) The influence of heat treatment on the thermomechanical response of Ni-rich NiTi alloys manufactured by selective laser melting. J Alloys Comp 677:204–210. https://doi.org/10.1016/j.jallcom.2016.03.161

29. Andani MT, Saedi S, Turabi AS, Karamooz MR, Haberland C, Karaca HE, Elahinia M (2017) Mechanical and shape memory properties of porous Ni50.1Ti49.9 alloys manufactured by selective laser melting. J Mech Behavior Biom Mater 68:224–231. https://doi.org/10.1016/j.jmbbm.2017.01.047

30. Saedi S, Moghaddam NS, Amerinatanzi A, Elahinia M, Karaca HE (2018) On the effects of selective laser melting process parameters on microstructure and thermomechanical response of Ni-rich NiTi. Acta Mater 144:552–560. https://doi.org/10.1016/j.actamat.2017.10.072

31. Meier H, Haberland C, Frenzel J (2011) Structural and functional properties of NiTi shape memory alloys produced by selective laser melting. In: Innovative developments in design and manufacturing: advanced research in virtual and rapid prototyping. Paulo Jorge Bartolo et al., Taylor and Francis Group, London pp 291–296.

32. Mazzoleni L, Demir AG, Caprio L, Pacher M, Previtali B (2020) Real-time observation of melt pool in selective laser melting: spatial, temporal and wavelength resolution criteria. IEEE Trans Instrum Meas 69(4):1179–1190. https://doi.org/10.1109/TIM.2019.2912236

33. Demir AG, Mazzoleni L, Caprio L, Patcher M, Previtali B (2019) Complementary use of pulsed and continuous wave emission modes to stabilize melt pool geometry in laser powder bed fusion. Opt Laser Technol 113:15–26. https://doi.org/10.1016/j.optlastec.2018.12.005

34. Kim J, Ji S, Yun Y-S, Yeo J-S (2018) A review: melt pool analysis for selective laser melting with continuous wave and pulse width modulated lasers. Appl Sci Converge Technol 27(6):113–119. https://doi.org/10.5757/ASCT.2018.27.6.113

35. Cherry JA, Davies HM, Mehemood S, Lavery NP, Brown SGR, Sienz J (2015) Investigation into the effect of process parameters on microstructural and physical properties of 316L stainless steel parts by selective laser melting. Int J Adv Manuf Technol 76:869–879. https://doi.org/10.1007/s00170-014-6297-2

36. Carfagni M (1998) The Loss Factor as a Measure of Mechanical Damping. Proc 16th International Modal Analysis Conference 1:580–584.

37. Duerig TW, Pelton AR (1994) Materials properties handbook: titanium alloys. ASM INTERNATIONAL, Materials Park, OH, pp 1035–1048